CONDENSED MATTER PHYSICS

Simultaneous implementation of resistive switching and rectifying effects in a metal-organic framework with switched hydrogen bond pathway

Zizhu Yao[1]*, Liang Pan[2]*, Lizhen Liu[1], Jindan Zhang[1], Quanjie Lin[1], Yingxiang Ye[1], Zhangjing Zhang[1†], Shengchang Xiang[1†], Banglin Chen[3†]

Resistive random-access memory (RRAM) has evolved as one of the most promising candidates for the next-generation memory, but bistability for information storage, simultaneous implementation of resistive switching and rectification effects, and a better understanding of switching mechanism are still challenging in this field. Herein, we report a RRAM device based on a chiral metal-organic framework (MOF) FJU-23-H_2O with switched hydrogen bond pathway within its channels, exhibiting an ultralow set voltage (~0.2 V), a high ON/OFF ratio (~10^5), and a high rectification ratio (~10^5). It is not only the first MOF with voltage-gated proton conduction but also the first single material showing both rectifying and resistive switching effects. By single-crystal x-ray diffraction analyses, the mechanism of the resistive switching has been demonstrated.

INTRODUCTION

In an era of big data, there is an urgent demand for designing high performance memory to address the exponential growth in data storage and computing needs. Resistive random-access memory (RRAM) (1–4) with high- and low-resistance states (HRS and LRS, respectively) to store bits of data, as a booming candidate for the next generation of memories, may open the way to neuromorphic and cognitive computing (5) because of its fast set/reset operation, low-power consumption, high-density storage, and good scaling capability. Ideal RRAMs, which should have high ON/OFF ratios of larger than 10 (the bigger the ratio, the better it is to simplify the signal amplifying circuit), low set voltage (to reduce power consumption), high endurance, and high storage density, are still under development (6). A wide range of materials have been explored as storage media for the RRAMs, mainly including inorganic oxides (7) and chalcogenides (8), organic polymers (9), and metal complexes (10). The inorganic media have good switching stability and ON/OFF ratio but suffer from high forming voltage/current and large set/reset voltage, while the polymer or metal complex media show high mechanical flexibility but inferior resistive switching (RS) performance. Although the nucleation and growth processes of conducting filaments can be monitored in some devices by means of conductive atomic force microscopy (11) or transmission electron microscopy (12), the switching mechanism for either inorganic or organic RRAMs is still unclear because of the random formation and the disorder arrangement of the carriers or the inherent structural complexities, leading to difficulties in performance optimization and stagnations in the development of the whole RRAMs field. It is a daunting challenge to realize a previously unidentified strategy to improve the RS performance with a better understanding of the RS mechanism.

Crossbar array with the smallest ideal cell area of $4F^2$ (F, minimum feature size) is the basic integration architecture in RRAM devices for high storage density. The inherent sneak path (13), the undesired current path flowing through the whole memory array, occurs when the target cell is programmed, which can cause writing disturbance, read accuracy degradation, and high-power consumption. It is usually alleviated by endowing the device with self-rectification or a selector, such as introducing 1D1R (one diode and one resistor)/1S1R (one selector and one resistor) structures (14, 15) or constructing multicomponent layers to create a Schottky barrier (16), but these composite methods inevitably decrease the integration level. Developing a single material simultaneously containing high RS performances and self-rectification to solve the contradiction between sneak path issue and integration level is impending. Metal-organic frameworks (MOFs) (17–20), a kind of porous crystalline materials constructed by metal centers and organic linkers, have emerged as an important platform for gas adsorption and separation (21), catalysis (22), and proton transport (23). The insulating skeletons and the regular channels serving as carrier transferring paths have enabled MOFs to be very promising materials for RRAMs. Their structural diversity allows optimizing RS performance by the adjustment of building blocks or post-modification. So far, the research on MOF RRAMs is still in its infancy, with only few examples reported (24–30). Although the Ag/ZIF-8/Si device (24) with the ON/OFF ratio of 10^7 and the set voltage of 1.2 V can be achieved by grafting the Ag filament into MOFs, the performance of other MOF RRAMs is not so good, with the ON/OFF ratio less than 10^3. Their RS mechanisms were speculated as conducting filaments (24), metal ion migration (27, 28), ferroelectric transition (26), oxidation or reduction process at insulator-electrode interface (25), and charge trapping (29, 30), but direct evidence is lacking. In this regard, the characteristics of crystallinity and structural visibility of MOF materials are very useful to reveal switching mechanism through the accurate observation of the dynamic structures of the carrier transport paths, although it has not been realized yet because of the highly chaotic guests in the MOF single crystals and/or the complexity of the MOF films.

Constructing bistability for information storage and realizing the rectification effect in MOFs are still a huge challenge. In this work,

[1]Fujian Provincial Key Laboratory of Polymer Materials, College of Chemistry and Materials Science, Fujian Normal University, 32 Shangsan Road, Fuzhou 350007, China. [2]School of Materials Science and Engineering, Nanyang Technological University, 50 Nanyang Avenue, Singapore 639798, Singapore. [3]Department of Chemistry, University of Texas at San Antonio, One UTSA Circle, San Antonio, TX 78249-0698, USA.
*These authors contributed equally to this work.
†Corresponding author. Email: zzhang@fjnu.edu.cn (Z.Z.); scxiang@fjnu.edu.cn (S.X.); banglin.chen@utsa.edu (B.C.)

a nonvolatile RRAM was fabricated on the basis of a new MOF $\{[ZnL(H_2O)]_3(H_2O)_4\}_n$ (FJU-23-H$_2$O, H$_2$L = 5-triazole isophthalic acid) with highly ordered lattice water molecules. Under the stimulation of various voltages, the varying proton conductivities in FJU-23-H$_2$O were observed, indicating HRS to LRS transitions. The FJU-23-H$_2$O also exhibits a rectification effect because of its unidirectional transport of protons, which can specifically identify electric field directions. FJU-23-H$_2$O is the first single material to exhibit both resistance and rectification effects with a high ON/OFF ratio, ultralow set voltage, and high rectification ratio. Through single-crystal x-ray diffraction (SCXRD) studies, the dynamic structures of proton transport paths in FJU-23-H$_2$O during switching process, have been extensively investigated to reveal the RS mechanism, in which its RS behavior originated from the turn ON/OFF of the switched hydrogen bond pathway under the stimulus of dc voltages.

RESULTS

Colorless bulk crystals FJU-23-H$_2$O were obtained through solvo-thermal reaction of mixed DMF (N,N'-dimethylformamide)/H$_2$O (3:2, v/v) solution of ZnNO$_3$.6H$_2$O and H$_2$L at 85°C for 1 day. SCXRD analyses reveal that FJU-23-H$_2$O crystallizes in the chiral hexagonal space group $P6_5$. There are three crystallographically independent Zn(II) atoms (Fig. 1, A to C), and each of them is coordinated with one water molecule and bridged by three fully deprotonated L^{2-} ligands to form the respective single honeycomb sheet containing hexagonal meshes of size ~7.04 Å by 10.18 Å (atom-to-atom distance; Fig. 1D). Four lattice water molecules encapsulated within
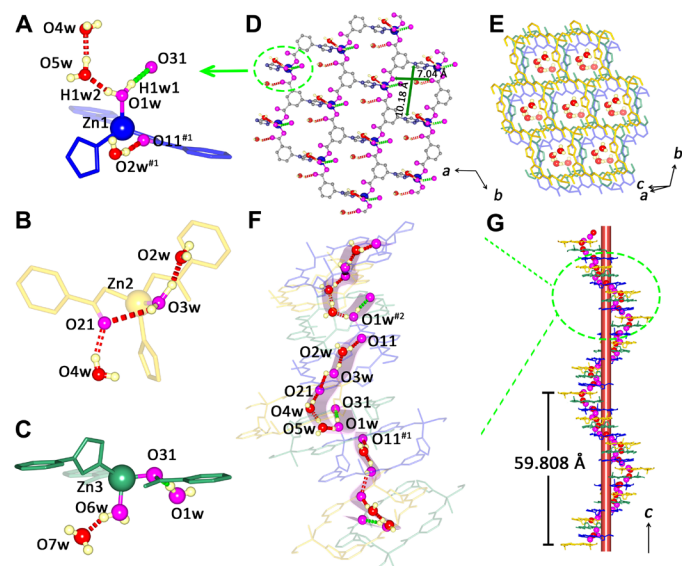

Fig. 1. The illustration of discontinuous hydrogen bonding chains in FJU-23-H$_2$O. (**A** to **C**) The hydrogen bonding interaction between the lattice water and the framework [color code for oxygen atoms: purple, located in the layer; red, out of the layer; d (O2w···O3w) = 2.688(8) Å; d (O3w···O21) = 3.005(7) Å; d (O21···O4w) = 2.675(9) Å; d (O1w···O5w) = 2.570(9) Å; d (O4w···O5w) = 2.614(10) Å]. (**D**) The single honeycomb sheet of Zn1 atoms. (**E**) Lattice water molecules located in hexagonal nanochannels of FJU-23-H$_2$O. (**F**) A hydrogen bonding chain fragment. (**G**) Three-dimensional stack for hydrogen bonding chain fragment along the c axis. Symmetry codes: (#1) −1+x, −1+y, z; (#2) x, −1+y, z; (#3) 1+x−y, x, −0.16667+z.

the hexagonal meshes are involved in the inter- and intrasheet O—H···O interactions with the coordination water and/or carboxylate O atoms, forming a self-assembled supramolecular three-dimensional framework containing helical channels to accommodate the lattice water (Fig. 1E). A distinguishing characteristic of FJU-23-H$_2$O is the presence of sixfold helices that align parallel to the c axis (Fig. 1, F and G, and fig. S1, A and B). Because the three single honeycomb sheets are noncoincident, sextuple stack in a parallel fashion affords an 18-sheet helical arrangement with a pitch of 59.808(12) Å. To the best of our knowledge, this is the highest level of stack yet observed in a net.

The most notable feature of FJU-23-H$_2$O structure is an incomplete hydrogen bond chain composed of short-range hydrogen bond fragments O11···O2w···O3w···O21···O4w···O5w···O1w···O31 in the helical channels (Fig. 1F). The O···O distances range from 2.570(9) to 3.102(8) Å, and the O—H···O angles range from 104.001(4)° to 170.789(6)°, being in the reasonable range of the hydrogen bonding interactions (31). Two hydrogen atoms (H1w1 and H1w2) riding on O1w were added based on the difference Fourier maps, and the DFIX command was used to restrain the O—H bond distances. The Zn1-coordinated water molecule (O1w) provides H1w2 atom to share with O5w, while it provides H1w1 atom to form another hydrogen bond with O31 of a neighboring isophthalate. The O1w···O31 distance is 3.102(8) Å, and the bond angle O1w—H1w1···O31 is 160.738(2)°. The large O1w···O11 distance of 3.189(8) Å and the small O1w—H1w1···O11 angle of 43.084(2)° suggest that no hydrogen bond is formed between O1w and O11 atoms, leading to the breakage of the hydrogen bonding chain between O1w and O11 atoms. However, the close distances of O1w···O31/O11 means that O31 and O11 are two competitive proton acceptors for the O1w—H1w1, especially under the external stimulus.

The short-range hydrogen bonding chain segments along the c axis in FJU-23-H$_2$O suggest the possibility of proton-conducting behavior. We measured the proton conductivity of FJU-23-H$_2$O single crystal along the a, b, or c axis by using ac impedance spectroscopy (Fig. 2A and fig. S1). All the Nyquist plots for the crystal sample along the c axis display a semicircle at high frequency, indicating its proton conduction (fig. S1C). The conductivity of FJU-23-H$_2$O along the c axis is 4.95×10^{-5} S/cm without an applied dc voltage. Upon increasing the dc voltages, the conductivity of FJU-23-H$_2$O is stuck on a kind of plateau of slow growth below 0.2 V. When the dc voltage is increased up to 0.2 V, a voltage-gated effect is observed and the conductivity sharply rises 32-fold, reaching 1.70×10^{-3} S/cm (Fig. 2B and fig. S1C), followed by another kind of plateau of slow increase up to the maximum dc voltage of 1 V. We applied the same measurement on FJU-23-H$_2$O crystal along the a and b axes, with no voltage-gated effect within the measured voltage range (fig. S1, D and E), suggesting that the hydrogen bonding helix is responsible for the conductive pathway along the c axis. To figure out the possible proton hopping mechanism, we measured the temperature-dependent ac impedance spectroscopy for FJU-23-H$_2$O along the c axis under the applied dc voltage of 0.1 or 0.5 V (fig. S1, F to H). On the basis of its typical Nyquist plots, the conductivity is improved with an increasing temperature, indicating the proton conduction rather than electron conduction. The least-square fit of the Arrhenius plots gave the corresponding activation energy values (E_a) of 0.42 and 1.42 eV, respectively. The proton-conduction mechanism in FJU-23-H$_2$O can be classified as the conventional vehicular mechanisms (32). To the best of our knowledge, FJU-23-H$_2$O is the first example of MOFs having the voltage-gated proton conduction, which prompts us to further explore its potential in the RRAM device.
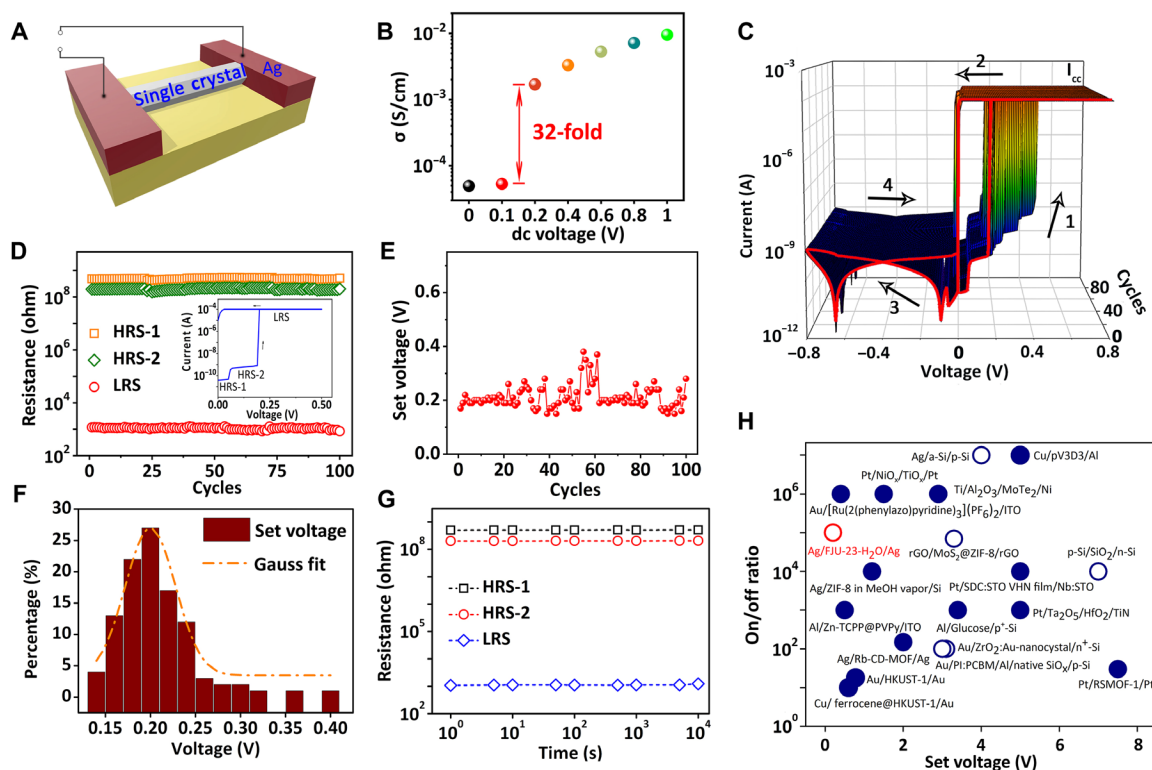
Fig. 2. Electrical performance of the device of FJU-23-H₂O single crystal along the *c* axis. (**A**) The illustration of electrical performance test. (**B**) Proton conductivity calculated from ac impedance spectroscopy for FJU-23-H₂O under ac voltage of 0.1 V and dc voltage range from 0 to 1 V at 294 K. (**C**) Semilogarithmic plot of the room-temperature *I-V* characteristics with 100 consecutive cycles. The red line represents the result of the first round of voltage sweeping. The arrows indicate the sweeping direction, while the numbers 1 to 4 represent the sweeping sequence. I_{CC} stands for the compliance current ($I_{CC} = 10^{-4}$ A). (**D**) Endurance performance, (**E**) the function of set voltage with the cycles, and (**F**) the histogram and Gaussian fitting curves of the distribution of the set voltage for the same device of one single crystal over 100 consecutive cycles. (**G**) Retention performance of the three conductance states over 10^4 s. The resistance of the sample was read at 0.05 V. (**H**) The comparison of the set voltage and ON/OFF ratio between FJU-23-H₂O and some representative RRAM materials, as presented in table S3 (symbol code: ○/●, the devices show the RS with and without rectifying effect).

After the test of ac impedance spectroscopy, we measured the dc current-voltage (*I-V*) curve on the same single crystal of FJU-23-H₂O (Fig. 2C). No RS has been observed for the devices of FJU-23-H₂O along *a* or *b* axis, as shown in fig. S1 (I and J). However, *I-V* curves of the device of FJU-23-H₂O along the *c* axis distinctly display three stable resistance states. A compliance current (I_{CC}) of 0.0001 A is used to prevent the breakdown of the device, and the general switching sequences are shown by the numbers included in Fig. 2C. The device initially stays at HRS-1 with a resistance of about 5.0×10^8 ohm. Upon increasing voltage, a small positive voltage of 0.07 V can turn the device from HRS-1 to HRS-2 with a resistance of about 2.0×10^8 ohm. When the dc voltage increases to 0.2 V, an abrupt increase of the device current to ~10^{-4} A is observed, indicating that the device has transited from the HRS-2 to the LRS. This off-to-on transition serves as the "set" process for a memory device, with an ON/OFF ratio as high as 10^5. The device remains in LRS, whether the voltage rises from 0.2 to 0.8 V or reduces from 0.8 to 0 V. A negatively sweeping voltage can reprogram the device to HRS-1, serving as the "reset" process of a rewritable memory. The almost identical shapes of the set curves suggest that no electroforming process is needed. Note that FJU-23-H₂O shows the higher current level at the positive bias than that at the negative bias with a rectification ratio of ~10^5 (read at ±0.5 V) (Fig. 2C), implying the nonvolatile and self-rectifying RS. To test the reliability of the memory device, we further examined the

endurance performance on the same device of one FJU-23-H₂O single crystal with the evolution of the resistance values of well-resolved HRS-1, HRS-2, and LRS in the 100 switching cycles (Fig. 2D). The ON/OFF ratio between HRS-2 and LRS remains more than 10^5 during the cyclic switching operation. The set voltage is not gradually increasing with cycles (Fig. 2E) but randomly distributed in the range of 0.14 to 0.4 V, mainly around 0.2 V (Fig. 2F). The device stays at the ON state after removing the power supply more than 10^4 s (Fig. 2G), suggesting the nonvolatile characteristics of the FJU-23-H₂O device again.

The FJU-23-H₂O device exhibits an ultralow set voltage (~0.2 V), a high rectification ratio (~10^5), and a high ON/OFF ratio (>10^5) under low I_{CC} (10^{-4} A). The RS parameters of the devices based on FJU-23-H₂O and some representative materials including the MOFs/coordination polymer (*10*, *24–30*), inorganic (*33–38*), and organic media (*39–41*) are listed in Fig. 2H and table S3 for comparison. First, the ON/OFF ratio of 10^5 for FJU-23-H₂O is higher than the values for most of the MOFs materials and comparable with the ones for some sophisticated inorganic oxides (*36*). Second, the FJU-23-H₂O device is electroforming-free with its set voltage of about 0.2 V, far lower than other ion transport–induced RRAMs, indicating that its switching mechanism cannot be assigned to metal ion migration. In general, a repeatable memristive switching behavior in nonproton ion transport–induced RRAMs is always

preceded by an electroforming step (*42*), and after that, a relatively high voltage is required to turn the device to LRS, which increases the operating power of the devices. The set voltage of the RRAM device is the same as the gate voltage, indicating that proton transport probably plays an important role in the RS. Using the proton with apparently smaller ionic radius and larger electromobility as the carriers may lead to the lower set voltage than the devices based on the migration of Ag^+ and OH^- ions. Last, the rectifying effect is observed in the MOF-based RRAMs, and FJU-23-H_2O is the first example of a single material exhibiting both rectifying and RS effects. Usually, the rectifying effect in the RRAMs is always realized by constructing the 1D1R/1T1R structure or adding external materials into media to create a Schottky barrier, which seems certain to reduce the interaction level and increase the power consumption of the device. On the basis of the *I-V* characteristic curves above, FJU-23-H_2O

can be regarded as a group of nonvolatile memristor and rectifier in the circuit.

Inspired by the voltage-gated proton-conducting effect and the self-rectifying and nonvolatile RS effects for the FJU-23-H_2O device, we further investigate its structural variation under various dc voltages on the same FJU-23-H_2O single crystal along the *c* axis, following the sequences as the points from 1 to 7 in Fig. 3A. On the basis of the retention time ($>10^4$ s), much longer than the time for collecting the structural data of FJU-23-H_2O, SCXRD was used to investigate the structural change in the same single crystal under various dc voltages. Although some advanced technologies have been used to observe ion transport under an electric field, SCXRD is first applied to get insight into the RS mechanism of RRAMs here. No substantial change has been observed in the framework or guest molecules of FJU-23-H_2O during this process, except for the switched O1w—H1w1···O31/O11
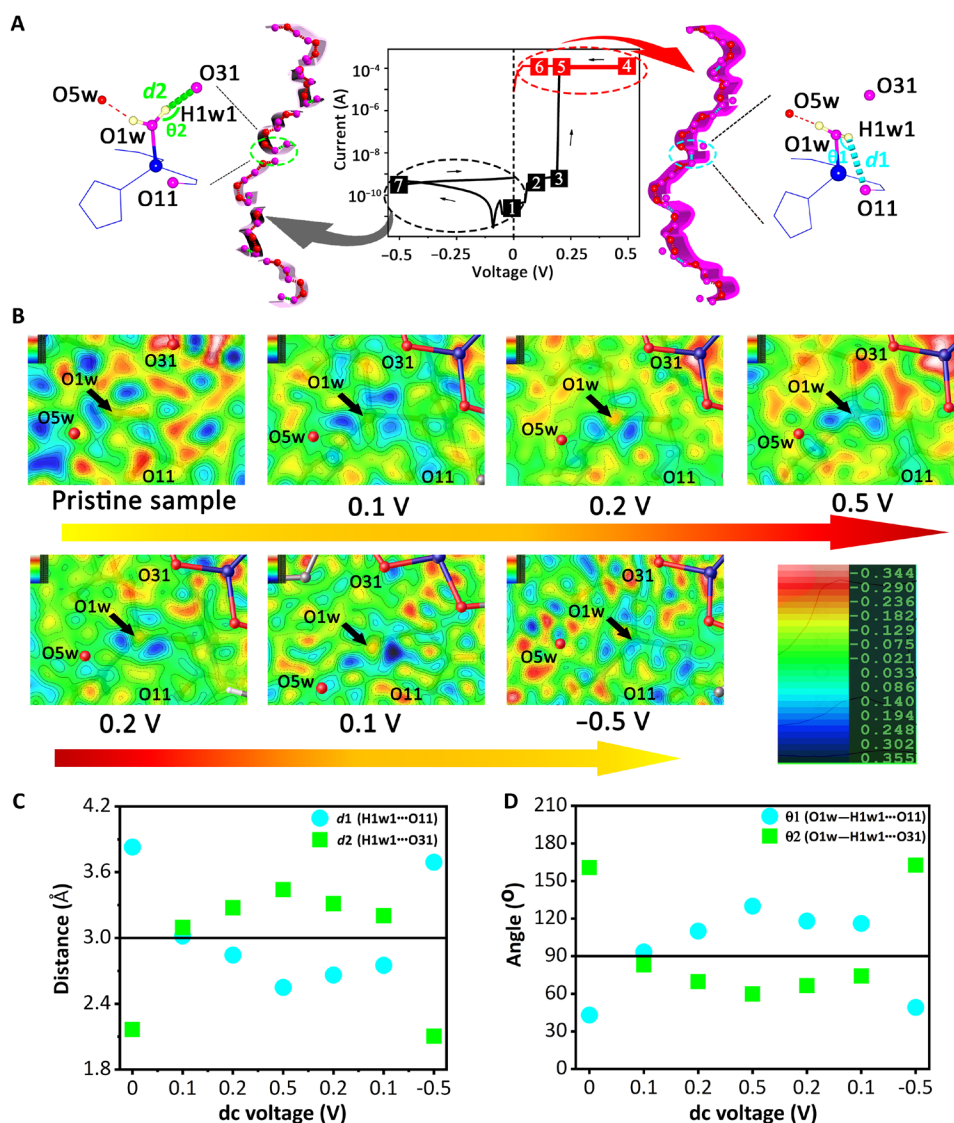
Fig. 3. Structural variation under various dc voltages applied on the same one single crystal of FJU-23-H₂O along the *c* axis. (**A**) The illustration of the applied dc voltages following the sequences as the points from 1 to 7. (**B**) The change of the electron density peaks near O1w in the original difference Fourier maps (diff) before adding H1w1 and H1w2 under the various dc voltages in the sequence above. The comparison of the distance *d* [H1w1(O1w)···O11] (*d1*) and *d* [H1w1(O1w)···O31] (*d2*) (**C**) and the bond angle θ (O1w—H1w1···O11) (*θ1*) and θ (O1w—H1w1···O31) (*θ2*) (**D**) in FJU-23-H₂O under various dc voltages.

interactions (Fig. 3 and fig. S3). The hydrogen atoms riding on O1w were added to the difference Fourier maps (Fig. 3B), and the DFIX command was used to restrain the O—H bond distances. As shown in the difference Fourier maps near O1w (Fig. 3B), one peak can be assigned to H1w2, which keeps forming hydrogen bonding interaction with O5w no matter how much the dc voltage applies, but the position of another peak (H1w1) obviously wiggles between O11 and O31. The distances between H1w1 and O11/O31 (denoted as $d1/d2$) and the angles O1w—H1w1$\cdots$O11/O31 (denoted as $\theta1/\theta2$) under various dc voltages are listed in Fig. 3 (C and D). Without an applied voltage, the electron density peak for H1w1 is oriented toward O31 with $d2$ of 2.165(3) Å and $\theta2$ of 160.738(2)°, but it departs from O11 with $d1$ of 3.830(3) and $\theta1$ of 43.084(2)°. The value of $\theta1$ is far lower than the threshold value of 90° (conservatively of 110°) for the normal hydrogen bonding interaction (*31*). The hydrogen bonding chains within the channels are partitioned into short-range hydrogen bond fragments by O1w—H1w1$\cdots$O31 interactions, leading to the HRS-1 state. When a dc voltage of 0.1 V is applied, two electron density peaks for H1w1 toward O11 and O31 are observed, respectively, with $d1/d2$ both close to 3.0 Å and $\theta1/\theta2$ to 90°. It means that hydrogen bonds of O1w—H1w1$\cdots$O31 and O1w—H1w1$\cdots$O11 simultaneously exist. Thus, the device switches from HRS-1 to HRS-2. Upon increasing the voltage to 0.5 V and then inversely sweeping to 0.2 and 0.1 V, the peak for H1w1 toward O11 is observed with the $\theta1 > 90°$ and the $d1 < 3.0$ Å. Upon bias, the O1w atom is torqued to break the original hydrogen bond with O31, instead forming a hydrogen bond with O11. This converts short hydrogen bonding fragments that were poised to interact with a complete hydrogen bonding helix that extends throughout the crystal. Thus, the device is in the LRS, which can still be retained upon the following smaller bias than the set voltage. The rectification effect is generated when a negative voltage is applied. The electron density peak for H1w1 atom comes back to O31 again upon −0.5 V dc voltage, with $\theta2/d2$ of 162.628(2)°/2.104(9) Å, respectively. The short-range hydrogen bonding fragments are recovered again, resulting in a reset from LRS to HRS-1. In conclusion, the electrical bistability of FJU-23-H$_2$O originates from the switching of O1w—H1w1$\cdots$O11/O31 hydrogen bonds driven upon the bias.

As a control experiment, FJU-23-D$_2$O was synthesized by a method similar to FJU-23-H$_2$O with D$_2$O instead of H$_2$O, which is isostructural to FJU-23-H$_2$O. According to the difference Fourier maps (fig. S4A), the electron density peaks near O1w are mainly oriented to O11 and O31 in FJU-23-D$_2$O (fig. S4, A and B), instead of O5w and O31 in FJU-23-H$_2$O. The electrical performance tests for FJU-23-D$_2$O were also executed along the c axis. In the I-V characteristics, it behaves just as a resistance without resistance switching and rectifying effect observed under the dc voltage from −10 to 10 V (fig. S4C). Upon expanding the dc voltage from −100 to 100 V, we also observed the resistance switching and rectifying effect but with a very large set voltage and a broad distribution from 56.5 to 99.5 V (fig. S4D). It is mainly because the H$^+$/D$^+$ ions as carriers play an important role in the resistance switching of MOFs. Compared with H$^+$, the increasing mass of D$^+$ leads to the lower ionic mobility and thus results in a drop in ionic conductivity and an increase in set voltage in FJU-23-D$_2$O. Moreover, its LRS cannot be retained when the applied dc voltage is quickly switched from 100 to 5 V (fig. S4E), confirmed by the currents of about 10^{-8} A at 5 V far less than the I_{CC} of 10^{-4} A of LRS at 100 V. It means that the resistance switching for FJU-23-D$_2$O is volatile. The volatile characteristic hinders us to test

the structures of FJU-23-D$_2$O under various dc voltages. In the ac impedance spectroscopy, we observed no voltage-gated proton conduction within the measured dc voltage range up to 40 V (fig. S4, F and G). It is reasonable to suggest that the voltage-gated effect can be observed in FJU-23-D$_2$O under the high set voltage more than 56.5 V. However, it is a pity that such a high dc voltage exceeds the working limits of 40 V for our impedance/gain-phase analyzer. The higher gate voltage and the lower current in FJU-23-D$_2$O than in FJU-23-H$_2$O suggest that the proton as a carrier plays an important role in the conductivity and resistance switching of FJU-23-H$_2$O.

DISCUSSION
The conductivity shown in FJU-23-H$_2$O along the c axis is inferred to be proton conduction based on the experiments and results mentioned above: (i) The ac impedance spectroscopy shows that the Nyquist plots display a semicircle at high frequency. (ii) The temperature-dependent impedance spectroscopy shows that the conductivity is improved with increasing temperature. (iii) The control experiments show the higher gate voltage and the lower current for FJU-23-D$_2$O than FJU-23-H$_2$O. (iv) The difference Fourier maps show that the bias-forced electrical bistability originates from the hydrogen atom on O1w switching between O11 and O31 atoms. Proton-conducting MOFs containing chiral proton channels with switched hydrogen bond pathway have great advantages as high-performance RRAM materials: (i) The proton carriers having smaller ionic radius and larger electromobility than other cationic or anionic carriers can reduce the set voltage to cut down energy consumption of the devices. (ii) The switched hydrogen bond pathway can impart the proton channels with voltage-gated effect and then increase the ON/OFF ratio of the devices. (iii) Asymmetric structure that originated from the chiral proton channel can endow the device with rectifying effect, as in the cases of the molecular rectifiers (*43*). Moreover, high-density storage is another important performance pursued by the semiconductor industry, and the characteristics of the long-range order of MOFs in microcosmic may provide a possibility for high-density storage. If we alternate FJU-23-H$_2$O's hexagonal channels as RRAM cell and its framework as shield, then an ultrahigh storage density of 17.5 TB/cm^2 can be realized, which is 100 times higher than the storage density of a traditional mechanical hard disk, although the corresponding integration technology still needs to be explored. Note that those proton-conducting MOF-based RRAMs involve MOFs and solid-state ionics to realize the on-demand regulation of resistance switching performance. Compared to traditional solid-state ionics subjected to purely inorganic materials, metal-organic solid ionics shows great advantage in regulating ion transport structure and in exploring the relationship between structures and properties, establishing the unambiguous role of metal-organic solid-state ionics in conducting devices.

In conclusion, we have observed a self-rectifying RRAM based on a single metal-organic material FJU-23-H$_2$O with the switched hydrogen bond pathway. The voltage-gated proton-conducting behavior in FJU-23-H$_2$O has been confirmed. The device exhibits an ultralow set voltage (~0.2 V), a high ON/OFF ratio (~10^5), and a high rectification ratio (~10^5), which is beneficial to reducing energy consumption, to simplifying signal amplifying circuit, and to alleviating sneak path issue in the device. By SCXRD, we demonstrate that the switching mechanism of FJU-23-H$_2$O is attributed to the turn ON/OFF

of the chiral proton channels with the switched hydrogen bond pathway under the stimulus of dc voltages, establishing the unambiguous role of metal-organic solid-state ionics in the conducting device.

MATERIALS AND METHODS
General remarks
All reagents and solvents were used as received from commercial suppliers without further purification. Thermogravimetric analysis (TGA) was performed on a Mettler Toledo TGA/SDTA851e analyzer in air with a heating rate of 5 K/min from 30 to 600°C. Elemental analysis was collected on vario EL elemental analyzer. Powder x-ray diffraction (PXRD) was carried out with a PANalytical X'Pert[3] powder diffractometer equipped with a Cu sealed tube ($\lambda = 1.54178$ Å) at 40 kV and 40 mA over the 2θ range of 5° to 30°. The *I-V* characteristics of FJU-23-H_2O and FJU-23-D_2O were measured on a Lakeshore probe station equipped with a precision semiconductor parameter analyzer (Keithley 4200) in dc sweep or pulse mode. The ligand H_2L and its precursor *N,N*-dimethylformamide azine dihydrochloride were synthesized according to the literature methods (*44, 45*).

Synthesis of FJU-23-H_2O and FJU-23-D_2O
A mixture of $Zn(NO_3)_2$·$6H_2O$ (0.1 mmol, 0.0297 g), H_2L (0.1 mmol, 0.0233 g), DMF (3 ml), and H_2O (2 ml) solution was stirred for 10 min. Then, the solution was transferred to a 23-ml glass jar and heated to 85°C. After 24 hours, the system was cooled to room temperature, and hexagonal prism colorless crystals were obtained (0.043 g, 42% yield with regard to H_2L): Cal C, 35.44%; H, 2.86%; N, 12.40%; found C, 35.38%; H, 2.91%; N, 12.42%. Some information on PXRD, TGA, and circular dichroism spectra for FJU-23-H_2O is listed in fig. S5. The FJU-23-D_2O crystals were synthesized in the same procedure as FJU-23-H_2O but with D_2O instead of H_2O. (0.016 g, 15.6% yield with regard to H_2L): Cal C, 34.98%; H, 1.45%; N, 12.23%; found C, 34.79%; H, 1.61%; N, 12.20%.

Single-crystal x-ray structure determination
The single-crystal data were collected on the Agilent Technologies SuperNova Single-Crystal Diffractometer equipped with graphite monochromatic Cu Kα radiation ($\lambda = 1.54184$ Å). Using Olex2 (*46*), the structures were solved with the Superflip structure solution program using charge flipping and refined with the SHELXL refinement package using least squares minimization. The hydrogen atoms on O1w and O3w were added to the difference Fourier maps, and the DFIX command was used to restrain the O─H bond distances. Other H atoms on lattice water were added geometrically and refined using the riding model because of the lack of Q peaks in the appropriate position around O atoms. Hydrogen atoms data on O1W and O3W were listed in tables S1 and S2, respectively.

Structure determination under various dc voltages was performed according to the following procedures below. One pristine single crystal of FJU-23-H_2O was placed on the probe station with a Keithley 4200 system and applied a dc voltage of 0.1 V along the *c* axis for 10 s. Then, it was mounted onto the SuperNova Diffractometer for collecting diffraction data to get the structure of FJU-23-0.1 V. Various dc voltages following the sequences of 0.2, 0.5, 0.2, 0.1, and −0.5 V were applied on the same single crystal along the *c* axis to get the structure of FJU-23-X [X = 0.2 V, 0.5 V, 0.2 V-R, 0.1 V-R, and (−) 0.5 V]. CCDC (Cambridge Crystallographic Data Centre) 1882640-1882647 and 1905466-1905467 contain the supplementary crystallographic data of FJU-23-H_2O, FJU-23-D_2O, FJU-23-0.1 V, FJU-23-0.2 V,

FJU-23-0.5 V, FJU-23-0.2 V-R, FJU-23-0.1 V-R, FJU-23-(−) 0.5 V, FJU-23-D_2O-150 k, and FJU-23-H_2O-293 k. These data can be obtained free of charge from the CCDC via www.ccdc.cam.ac.uk/data_request/cif.

Electrical performance test
The glass substrates were precleaned sequentially with ethanol, acetone, and isopropanol in an ultrasonic bath, each for 20 min. A single crystal of FJU-23-H_2O with approximate dimensions of 0.003 cm (edge length of the six prism bottom) by 0.003 cm (edge length of the six prism bottom) by 0.019 cm was selected and placed onto the glass substrate along the *c* axis. The crystal was coated on the two hexagon sides with silver conducting glue. Then, the glass was put into the Lakeshore CRX-VF Cryogenic Probe Station (fig. S2). Two tungsten tips with a diameter of 20 μm were in direct contact with the silver conducting glue, serving as the electrode. An ac voltage of 0.1 V accompanying with various dc voltages was applied on the sample to test impedance spectroscopy at the probe station with a 1296 dielectric interface impedance analyzer. The *I-V* curve on the same single crystal of FJU-23-H_2O along the *c* axis was measured further at the probe station with a Keithley 4200 semiconductor characterization system in voltage-sweeping mode, instead of the impedance analyzer. The sensitivity of the Keithley 4200 system was 10 fA. During the *I-V* measurements, a bias voltage was applied through the tungsten tip with a sweeping step of 0.01 V. An I_{CC} preset of 10^{-4} A was used to avoid overstriking or permanent breakdown of the sample. The similar measurement was applied to one FJU-23-D_2O single crystal in the size of 0.0045 cm by 0.0045 cm by 0.0125 cm.

SUPPLEMENTARY MATERIALS
Supplementary material for this article is available at http://advances.sciencemag.org/cgi/content/full/5/8/eaaw4515/DC1

Fig. S1. Structure and electrical performance of FJU-23-H_2O single crystal.
Fig. S2. The microscopic image of the experimental setup.
Fig. S3. Variations of distance (H1w1···O31) and bond angle (O1w—H1w1···O11) under various dc voltages applied on the same one single crystal of FJU-23-H_2O along the *c* axis.
Fig. S4. Structure and electrical performance of FJU-23-D_2O single crystal.
Fig. S5. The characterization of FJU-23-H_2O.
Table S1. Selected bond lengths (Å) and bond angles (°) for O1w.
Table S2. Selected bond lengths (Å) and bond angles (°) for O3w.
Table S3. Performance parameters for some representative RRAMs.
Table S4. Crystal data and structure refinement for FJU-23-H_2O, FJU-23-D_2O, and FJU-23-H_2O under voltage sweeping on one single crystal.

REFERENCES AND NOTES
1. International Roadmap for Devices and Systems, Emerging research materials (IRDS, 2017); https://irds.ieee.org/images/files/pdf/2017/2017IRDS_ERM.pdf.
2. D. B. Strukov, G. S. Snider, D. R. Stewart, R. S. Williams, The missing memristor found. *Nature* **453**, 80–83 (2008).
3. R. Waser, M. Aono, Nanoionics-based resistive switching memories. *Nat. Mater.* **6**, 833–840 (2007).
4. S. Gao, X. Yi, J. Shang, G. Liu, R. W. Li, Organic and hybrid resistive switching materials and devices. *Chem. Soc. Rev.* **48**, 1531–1565 (2019).
5. M. Prezioso, F. Merrikh-Bayat, B. D. Hoskins, G. C. Adam, K. K. Likharev, D. B. Strukov, Training and operation of an integrated neuromorphic network based on metal-oxide memristors. *Nature* **521**, 61–64 (2015).
6. F. Pan, S. Gao, C. Chen, C. Song, F. Zeng, Recent progress in resistive random access memories: Materials, switching mechanisms, and performance. *Mater. Sci. Eng. R Rep.* **83**, 1–59 (2014).
7. H. Jiang, D. Belkin, S. E. Savel'ev, S. Lin, Z. Wang, Y. Li, S. Joshi, R. Midya, C. Li, M. Rao, M. Barnell, Q. Wu, J. J. Yang, Q. Xia, A novel true random number generator based on a stochastic diffusive memristor. *Nat. Commun.* **8**, 882 (2017).
8. M. Kim, R. Ge, X. Wu, X. Lan, J. Tice, J. C. Lee, D. Akinwande, Zero-static power radio-frequency switches based on MoS_2 atomristors. *Nat. Commun.* **9**, 2524 (2018).

9. Y. van de Burgt, E. Lubberman, E. J. Fuller, S. T. Keene, G. C. Faria, S. Agarwal, M. J. Marinella, A. A. Talin, A. Salleo, A non-volatile organic electrochemical device as a low-voltage artificial synapse for neuromorphic computing. *Nat. Mater.* **16**, 414–419 (2017).

10. S. Goswami, A. J. Matula, S. P. Rath, S. Hedström, S. Saha, M. Annamalai, D. Sengupta, A. Patra, S. Ghosh, H. Jani, S. Sarkar, M. R. Motapothula, C. A. Nijhuis, J. Martin, S. Goswami, V. S. Batista, T. Venkatesan, Robust resistive memory devices using solution-processable metal-coordinated azo aromatics. *Nat. Mater.* **16**, 1216–1224 (2017).

11. K. Kinoshita, T. Okutani, H. Tanaka, T. Hinoki, K. Yazawa, K. Ohmi, S. Kishida, Opposite bias polarity dependence of resistive switching in *n*-type Ga-doped-ZnO and *p*-type NiO thin films. *Appl. Phys. Lett.* **96**, 143505 (2010).

12. Y. Yang, P. Gao, S. Gaba, T. Chang, X. Pan, W. Lu, Observation of conducting filament growth in nanoscale resistive memories. *Nat. Commun.* **3**, 732 (2012).

13. E. Linn, R. Rosezin, C. Kügeler, R. Waser, Complementary resistive switches for passive nanocrossbar memories. *Nat. Mater.* **9**, 403–406 (2010).

14. G. H. Kim, J. H. Lee, Y. Ahn, W. Jeon, S. J. Song, J. Y. Seok, J. H. Yoon, K. J. Yoon, T. J. Park, C. S. Hwang, 32 × 32 crossbar array resistive memory composed of a stacked Schottky diode and unipolar resistive memory. *Adv. Funct. Mater.* **23**, 1440–1449 (2013).

15. W. Xue, G. Liu, Z. Zhong, Y. Dai, J. Shang, Y. Liu, H. Yang, X. Yi, H. Tan, L. Pan, S. Gao, J. Ding, X. Xu, R.-W. Li, A 1D vanadium dioxide nanochannel constructed via electric-field-induced ion transport and its superior metal-insulator transition. *Adv. Mater.* **29**, 1702162 (2017).

16. J. H. Yoon, S. Yoo, S. J. Song, K. J. Yoon, D. E. Kwon, Y. J. Kwon, T. H. Park, H. J. Kim, X. L. Shao, Y. Kim, C. S. Hwang, Uniform self-rectifying resistive switching behavior via preformed conducting paths in a vertical-type Ta_2O_5/HfO_{2-x} structure with a sub-μm^2 cell area. *ACS Appl. Mater. Interfaces* **8**, 18215–18221 (2016).

17. A. Schoedel, M. Li, D. Li, M. O'Keeffe, O. M. Yaghi, Structures of metal-organic frameworks with rod secondary building units. *Chem. Rev.* **116**, 12466–12535 (2016).

18. J. E. Mondloch, M. J. Katz, W. C. Isley III, P. Ghosh, P. L. Liao, W. Bury, G. Wagner, M. G. Hall, J. B. DeCoste, G. W. Peterson, R. Q. Snurr, C. J. Cramer, J. T. Hupp, O. K. Farha, Destruction of chemical warfare agents using metal-organic frameworks. *Nat. Mater.* **14**, 512–516 (2015).

19. P. Q. Liao, N. Y. Huang, W. X. Zhang, J. P. Zhang, X. M. Chen, Controlling guest conformation for efficient purification of butadiene. *Science* **356**, 1193–1196 (2017).

20. Q. G. Zhai, X. Bu, X. Zhao, D. S. Li, P. Feng, Pore space partition in metal-organic frameworks. *Acc. Chem. Res.* **50**, 407–417 (2017).

21. H. Sato, W. Kosaka, R. Matsuda, A. Hori, Y. Hijikata, R. V. Belosludov, S. Sakaki, M. Takata, S. Kitagawa, Self-accelerating CO sorption in a soft nanoporous crystal. *Science* **10**, 167–170 (2014).

22. C. S. Diercks, Y. Liu, K. E. Cordova, O. M. Yaghi, The role of reticular chemistry in the design of CO$_2$ reduction catalysts. *Nat. Mater.* **17**, 301–307 (2018).

23. G. K. H. Shimizu, J. M. Taylor, S. Kim, Proton conduction with metal-organic frameworks. *Science* **26**, 354–355 (2013).

24. Y. Liu, H. Wang, W. X. Shi, W. N. Zhang, J. C. Yu, B. K. Chandran, C. L. Cui, B. W. Zhu, Z. Y. Liu, B. Li, C. Xu, Z. L. Xu, S. Z. Li, W. Huang, F. W. Huo, X. D. Chen, Alcohol-mediated resistance-switching behavior in metal-organic framework-based electronic devices. *Angew. Chem. Int. Ed.* **55**, 8884–8888 (2016).

25. S. M. Yoon, S. C. Warren, B. A. Grzybowski, Storage of electrical information in metal-organic-framework memristors. *Angew. Chem.* **126**, 4526–4530 (2014).

26. L. Pan, G. Liu, H. Li, S. Meng, L. Han, J. Shang, B. Chen, A. E. Platero-Prats, W. Lu, X. D. Zou, R. W. Li, A resistance-switchable and ferroelectric metal-organic framework. *J. Am. Chem. Soc.* **136**, 17477–17483 (2014).

27. Z. Wang, D. Nminibapiel, P. Shrestha, J. Liu, W. Guo, P. G. Weidler, H. Baumgart, C. Wöll, E. Redel, Resistive switching nanodevices based on metal-organic frameworks. *ChemNanoMat* **2**, 67–73 (2016).

28. L. Pan, Z. Ji, X. Yi, X. Zhu, X. Chen, J. Shang, G. Liu, R.-W. Li, Metal-organic framework nanofilm for mechanically flexible information storage applications. *Adv. Funct. Mater.* **25**, 2677–2685 (2015).

29. X. Huang, B. Zheng, Z. D. Liu, C. L. Tan, J. Q. Liu, B. Chen, H. Li, J. Z. Chen, X. Zhang, Z. X. Fan, W. N. Zhang, Z. Guo, F. W. Huo, Y. H. Yang, L. H. Xie, W. Huang, H. Zhang, Coating two-dimensional nanomaterials with metal-organic frameworks. *ACS Nano* **8**, 8695–8701 (2014).

30. G. Ding, Y. Wang, G. Zhang, K. Zhou, K. Zeng, Z. Li, Y. Zhou, C. Zhang, X. Chen, S.-T. Han, 2D metal-organic framework nanosheets with time-dependent and multilevel memristive switching. *Adv. Funct. Mater.* **29**, 1806637 (2018).

31. T. Steiner, The hydrogen bond in the solid state. *Angew. Chem. Int. Ed.* **41**, 48–76 (2002).

32. Y. Ye, W. Guo, L. Wang, Z. Li, Z. Song, J. Chen, Z. Zhang, S. Xiang, B. Chen, Straightforward loading of imidazole molecules into metal-organic framework for high proton conduction. *J. Am. Chem. Soc.* **139**, 15604–15607 (2017).

33. J. H. Yoon, S. J. Song, I. H. Yoo, J. Y. Seok, K. J. Yoon, D. E. Kwon, T. H. Park, C. S. Hwang, Highly uniform, electroforming-free, and self-rectifying resistive memory in the Pt/Ta_2O_5/HfO_{2-x}/TiN structure. *Adv. Funct. Mater.* **24**, 5086–5095 (2015).

34. S. H. Jo, W. Lu, CMOS compatible nanoscale nonvolatile resistance switching memory. *Nano Lett.* **8**, 392–397 (2008).

35. Q. Y. Zuo, S. B. Long, Q. Liu, S. Zhang, Q. Wang, Y. T. Li, Y. Wang, M. Liu, Self-rectifying effect in gold nanocrystal-embedded zirconium oxide resistive memory. *J. Appl. Phys.* **106**, 073724 (2009).

36. M. J. Lee, S. Seo, D.-C. Kim, S. E. Ahn, D. H. Seo, I.-K. Yoo, I.-G. Baek, D. S. Kim, I. S. Byun, S.-H. Kim, I.-R. Hwang, J.-S. Kim, S.-H. Jeon, B. H. Park, A low-temperature-grown oxide diode as a new switch element for high-density, nonvolatile memories. *Adv. Mater.* **19**, 73–76 (2007).

37. S. Cho, C. Yun, S. Tappertzhofen, A. Kursumovic, S. Lee, P. Lu, Q. Jia, M. Fan, J. Jian, H. Wang, S. Hofmann, J. MacManus-Driscoll, Self-assembled oxide films with tailored nanoscale ionic and electronic channels for controlled resistive switching. *Nat. Commun.* **7**, 12373 (2016).

38. C. Li, L. Han, H. Jiang, M.-H. Jang, P. Lin, Q. Wu, M. Barnell, J. J. Yang, H. L. Xin, Q. Xia, Three-dimensional crossbar arrays of self-rectifying Si/SiO_2/Si memristors. *Nat. Commun.* **8**, 15666 (2015).

39. B. Cho, T. W. Kim, S. Song, Y. Ji, M. Jo, H. Hwang, G. Y. Jung, T. Lee, Rewritable switching of one diode–one resistor nonvolatile organic memory devices. *Adv. Mater.* **22**, 1228–1232 (2010).

40. S. P. Park, Y. J. Tak, H. J. Kim, J. H. Lee, H. Yoo, H. J. Kim, Analysis of the bipolar resistive switching behavior of a biocompatible glucose film for resistive random access memory. *Adv. Mater.* **30**, 1800722 (2018).

41. B. C. Jang, H. Seong, S. K. Kim, J. Y. Kim, B. J. Koo, J. Choi, S. Y. Yang, S. G. Im, S. Y. Choi, Flexible nonvolatile polymer memory array on plastic substrate via initiated chemical vapor deposition. *ACS Appl. Mater. Interfaces* **8**, 12951–12958 (2016).

42. K. M. Kim, J. Zhang, C. Graves, J. J. Yang, B. J. Choi, C. S. Hwang, Z. Li, R. S. Williams, Low-power, self-rectifying, and forming-free memristor with an asymmetric programing voltage for a high-density crossbar application. *Nano Lett.* **16**, 6724–6732 (2016).

43. X. Chen, M. Roemer, L. Yuan, W. Du, D. Thompson, E. D. Barco, C. A. Nijhuis, Molecular diodes with rectification ratios exceeding 10^5 driven by electrostatic interactions. *Nat. Nanotechnol.* **12**, 797–803 (2017).

44. Z. Yao, Z. Zhang, L. Liu, Z. Li, W. Zhou, Y. Zhao, Y. Han, B. Chen, R. Krishna, S. Xiang, Extraordinary separation performance towards acetylene containing mixtures on microporous MOFs with open O donor sites and tunable robustness via control of helical chains SBUs. *Chem. A Eur. J.* **22**, 5676–5683 (2016).

45. T. Panda, T. Kundu, R. Banerjee, Self-assembled one dimensional functionalized metal–organic nanotubes (MONTs) for proton conduction. *Chem. Commun.* **48**, 5464–5466 (2012).

46. O. V. Dolomanov, L. J. Bourhis, R. J. Gildea, J. A. K. Howard, H. Puschmann, *OLEX2*: A complete structure solution, refinement and analysis program. *J. Appl. Cryst.* **42**, 339–341 (2009).

Citation: Z. Yao, L. Pan, L. Liu, J. Zhang, Q. Lin, Y. Ye, Z. Zhang, S. Xiang, B. Chen, Simultaneous implementation of resistive switching and rectifying effects in a metal-organic framework with switched hydrogen bond pathway. *Sci. Adv.* **5**, eaaw4515 (2019).